Diffuse scattered field of elastic waves from randomly rough surfaces using an analytical Kirchhoff theory

F. Shi[a,*], M. J. S. Lowe[a], X. Xi[a], R. V. Craster[b]

[a] *Department of Mechanical Engineering, Imperial College London*
[b] *Department of Mathematics, Imperial College London*

Abstract

We develop an elastodynamic theory to predict the diffuse scattered field of elastic waves by randomly rough surfaces, for the first time, with the aid of the Kirchhoff approximation (KA). Analytical expressions are derived incorporating surface statistics, to represent the expectation of the angular distribution of the diffuse intensity for different modes. The analytical solutions are successfully verified with numerical Monte Carlo simulations, and also validated by comparison with experiments. We then apply the theory to quantitatively investigate the effects of the roughness and the shear-to-compressional wave speed ratio on the mode conversion and the scattering intensity, from low to high roughness within the valid region of KA. Both the direct and the mode converted intensities are significantly affected by the roughness, which leads to distinct scattering patterns for different wave modes. The mode conversion effect is very strong around the specular angle and it is found to increase as the surface appears to be more rough. In addition, the 3D roughness induced coupling between the out-of-plane shear horizontal (SH) mode and the in-plane modes is studied. The intensity of the SH mode is shown to be very sensitive to the out-of-plane correlation length, being influenced more by this than by the RMS value of the roughness. However, it is found that the depolarization pattern for the diffuse field is independent of the actual value of the roughness.

*Corresponding author.
E-mail address: f.shi12@imperial.ac.uk

Keywords: Diffuse scattered waves, Elastic waves, Randomly rough surface, Kirchhoff approximation

1. Introduction

Elastic wave scattering from a surface is significantly affected by its roughness (Ogilvy, 1991). How the surface roughness changes the expected scattering intensity, and its angular distribution, is a fundamental problem which has remained open. The applications vary from boundary scattering of phonons for thermal transport relevant for terahertz elastic phonon devices (Sun and Pipe, 2012; Maznev, 2015), ultrasound detection/imaging (Ogilvy and Culverwell, 1991; Zhang et al., 2012) for Non-Destructive Evaluation (NDE), to seismic wave exploration at infrasonic frequencies (Robertsson et al., 2006). All of these problems share similar wave scattering theory mathematically (e.g. $2nd$-order elastic wave equation) although with different scales of the wavelength.

Figure 1 shows a schematic of the scattering problem, for the two-dimensional and three-dimensional cases. These show a plane wave incident at an arbitrary angle at a rough surface. The resulting scattered waves are composed of contributions from different points along the surface, which interfere constructively or destructively, producing reflections and mode conversions over a range of angles. The unit incident and the scattering vectors in 2D are denoted as:

$$\begin{aligned} \hat{\boldsymbol{k}}_{\boldsymbol{in}} &= (\sin\theta_i, -\cos\theta_i) \\ \hat{\boldsymbol{k}}_{\boldsymbol{sc}} &= (\sin\theta_s, \cos\theta_s) \end{aligned} \tag{1}$$

and in 3D as:

$$\begin{aligned} \hat{\boldsymbol{k}}_{\boldsymbol{in}} &= (-\sin\theta_{iz}\cos\theta_{ix}, -\sin\theta_{iz}\sin\theta_{ix}, -\cos\theta_{iz}) \\ \hat{\boldsymbol{k}}_{\boldsymbol{sc}} &= (\sin\theta_{sz}\cos\theta_{sx}, \sin\theta_{sz}\sin\theta_{sx}, \cos\theta_{sz}) \end{aligned} \tag{2}$$

where the angles θ_i, θ_s are the incident and scattered angles respectively, and are shown in Figure 1.

We are interested in predicting the scattering that occurs at a rough surface of a defect, such as a crack, for applications in NDE. Specific geometries of cracks are rarely known, but it is often the case that the expected statistics of the roughness can be obtained, such that an answer by way of a statistical expectation of the scattering is useful to justify an expected sensitivity of a proposed inspection. This is typically seen as the pursuit of a basis to say that the scattering amplitude will exceed a certain threshold in any given case. Early works with this in mind, led by Ogilvy (1986), investigated the coherent scattering intensity at the specular angle via a decay factor $g_{\alpha\beta}$ defined through:

$$I_c = I^{fs} \exp(-g_{\alpha\beta}), \qquad \alpha, \beta = p, s \tag{3}$$

where p, s denotes compressional and shear components respectively with the first letter corresponding to the incident wave-type and the second to that being measured. In (3) I_{fs} is the response from a flat surface with the same dimension. In 2D the decay factor $g_{\alpha\beta} = (k_\alpha + k_\beta)^2 \cos\theta_i^2 \sigma^2$, where $k_{\alpha/\beta}$ represents the wavenumber for incident/scattered waves. Equation (3) is a single expression for the reduction of the coherent intensity due to the increase of the surface RMS value σ. The coherent intensity is the intensity that would be found by averaging the scattered signals from a large number of realizations of the roughness of the given statistical description; this is used widely in justification for inspections of safety-critical components in industry (Pettit et al., 2015). However, it is also known that this approach is very conservative for high roughness and non-specular angles (Ogilvy, 1991, 1986; Sun and Pipe, 2012), since the diffuse field, which is often the dominant part, is not included in the equation. In practice it would be highly desirable to obtain a value of the scattering that includes the contribution of the diffuse field, because in a single realization in a real setup (e.g. a single NDE measurement) it is not just the coherent intensity that is measured but rather some addition of coherent and diffuse parts; this is better described as the expected value of the scattering intensity (Pettit et al., 2015). Only a rough estimation of the elastodynamic diffuse intensity is

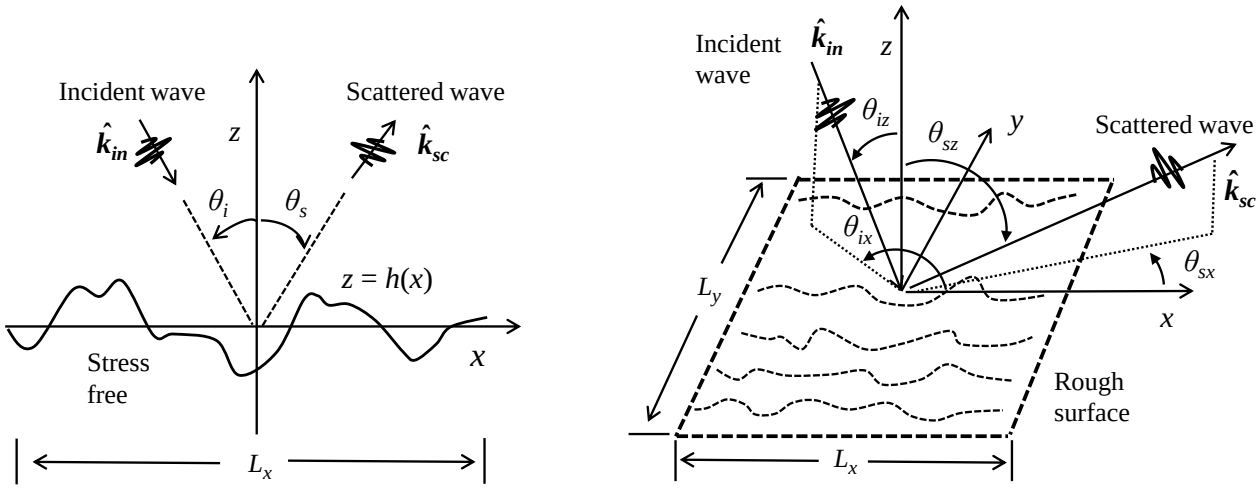

Figure 1: Sketch of a plane wave scattered from a rough surface. (a) 2D. (b) 3D.

currently given in the literature (Ogilvy, 1991, 1986), due to lack of knowledge, for the full calculation.

More recently, sophisticated numerical techniques have been adopted to study elastic waves scattered from randomly rough surfaces (Roberts, 2012; Jarvis and Cegla, 2012; Zhang et al., 2011; Shi et al., 2015; Pettit et al., 2015) with different applications in NDE. In (Pettit et al., 2015), the diffuse field has been calculated by FE simulations using the Monte Carlo approach. Their work delivered a numerical solution for the expected coherent and diffuse back-scatter at normal incidence, from which it was possible to propose a very significant erosion of the conservatism in the present inspection procedures. However, as is well known, the numerical methods are computationally expensive, and it is not straightforward to find the connection between the surface statistics and the scattering field from purely numerical results. Analytical methods provide alternative ways to obtain simple mathematical expressions for a rapid calculation of the intensity. More importantly they enable a direct incorporation of the statistical parameters of the surface into the formulae, so that the intrinsic

relation between the roughness and the diffuse intensity can additionally be revealed.

For example, the perturbation approach (Harper and Labianca, 1975; Thorsos and Jackson, 1989) and the Kirchhoff approximation (KA) (Eckart, 1953; Thorsos, 1988, 1990) have been extensively applied to study acoustic wave scattering. However, very few theoretical studies can be found for the diffuse elastic wave scattering from randomly rough surfaces. One of the most recent works involves the perturbation analysis of elastic phonon scattering from a rough surface in a solid medium (Maznev, 2015). However, it is known that the perturbation approach is only valid for weakly rough surfaces, for instance $\sigma < \lambda/10$ (σ being the RMS height for the roughness and λ a wavelength of the incident field) if only considering the first-order approximation (Thorsos and Jackson, 1989). In the field of NDE and seismology, the RMS value for cases of interest typically has a much larger range approximately from $\lambda/20$ upto $\lambda/3$ (Ogilvy, 1986; Zhang et al., 2012; Makinde et al., 2005) where the perturbation method might not be reliable.

By contrast, KA can handle scattering from surfaces with roughness up to $\sigma = \lambda/3$ according to recent studies (Zhang et al., 2011; Shi et al., 2015). At such high roughness the scattering pattern is completely different from that with a weakly rough surface: At high roughness the diffuse field is dominant and the scattering energy is more isotropically distributed over the angular range. Such a theory using the Kirchhoff approximation is found for acoustic waves (Thorsos and Jackson, 1989; Beckmann and Spizzichino, 1987), by applying Beckmann's slope approximation derived from integration by parts. But for decades the counterpart analytical expression has not been found for elastic waves, with the stumbling block being the mode coupling at the rough boundary as mentioned by Ogilvy (1991). The local reflection coefficient/amplitude varies with respect to the surface gradient for elastic waves, so that one requires the two-point height-gradient average that is not generally known (Ogilvy, 1986). The elasto-

dynamic setting fundamentally differs from that of acoustic waves mainly due to the mode conversion and the polarization, which are unique for elastic waves, that are also heavily influenced by the roughness of the surface.

We proceed to overcome these obstacles and derive theoretical formulae to represent the elastic wave diffuse intensity with the KA for different modes. We consider an incident compressional (P) wave scattering into compressional and mode-converted shear (S) waves, and include three dimensional considerations. The formulae, presented for both 2D and 3D representations, are valid for arbitrary choices of the angle of the incident wave and the roughness, within the range of validity of KA. For brevity, the cases of incident shear wave are not presented, but follow a similar derivation. The theory we develop here enables us to perform a theoretical investigation of the effect of roughness on the mode conversion.

This article is organized as follows: Section II introduces the statistical profile of rough surfaces. Section III describes the derivation of the theoretical formulae and the high frequency asymptotic solution, including the slope approximations for different wave modes and the statistical treatment of the ensemble averaging. The developed theory is verified by numerical Monte Carlo simulations in Section IV, and experiments are performed to further validate the theory in Section V. Section VI presents a systematic physical analysis for the effect of the roughnesses and elasticity on the mode conversion and the scattering intensity. The term elasticity is used here to indicate the degree to which the problem is an elastic one rather than an acoustic one, and this is expressed as the shear-to-compressional wave speed ratio; when this ratio is zero, we have an acoustic problem, when it is high we have a problem for which there will be strong expressions of the behavior that we identify as characteristic of elastic wave scattering, such as mode conversions. The out-of-plane depolarization induced by the 3D roughness is also investigated for the first time. Concluding remarks are made in Section VII.

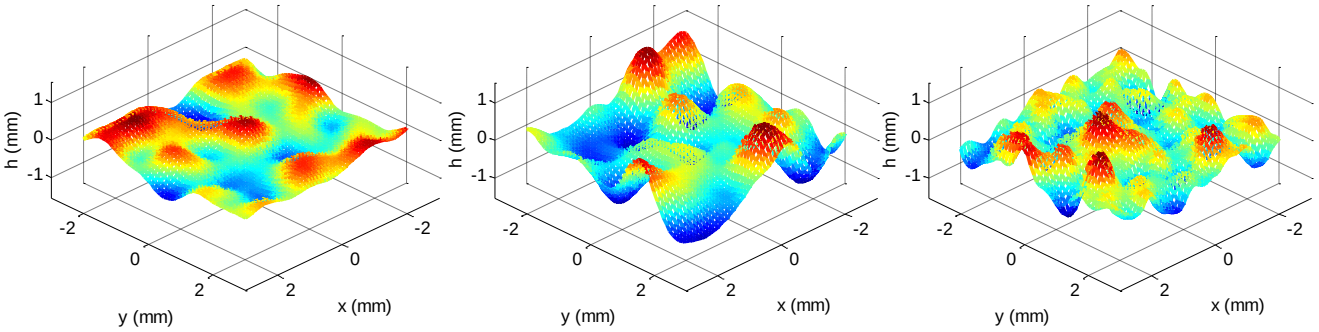

Figure 2: 3D isotropic Gaussian rough surface profiles. (a) $\sigma = 0.26$mm, $\lambda_0 = 0.77$mm. (b) $\sigma = 0.51$mm, $\lambda_0 = 0.77$mm. (c) $\sigma = 0.26$mm, $\lambda_0 = 0.39$mm.

2. Rough surface

The surface is defined as 'rough' in the sense that the surface height data is described by some statistical model. For instance, the probability density function (pdf) of the height for a Gaussian surface is expressed as:

$$p(h) = \frac{1}{\sigma\sqrt{2\pi}} \exp\left(-\frac{h^2}{2\sigma^2}\right) \tag{4}$$

The mean value is always assumed to be zero, and the RMS height σ according to definition is:

$$\sigma = \sqrt{< h^2 >} = \sqrt{\frac{1}{N}\sum_{i=1}^{N} h_i^2}. \tag{5}$$

where $<>$ denotes the ensemble averaging. The RMS value determines the height scale of the surface. In addition, a correlation function $W(\boldsymbol{R})$ is needed for the lateral variation of the height, and it is often assumed to be Gaussian:

$$W(\boldsymbol{R}) = \frac{< h(\boldsymbol{r})h(\boldsymbol{r}+\boldsymbol{R}) >}{\sigma^2} = \exp\left[-\left(\frac{x^2}{\lambda_x^2} + \frac{y^2}{\lambda_y^2}\right)\right]. \tag{6}$$

where λ_x and λ_y are called the correlation lengths in the x- and y- directions, as distances over which the correlation function falls by $1/e$. It is also known

that for a surface whose height pdf is a Gaussian, the distribution of the surface gradient p_g is also Gaussian (Ogilvy, 1988):

$$p_g\left(\frac{\partial h}{\partial x}\right) = \frac{1}{\sigma_g\sqrt{2\pi}}\exp\left[-\frac{(\frac{\partial h}{\partial x})^2}{2\sigma_g^2}\right], \qquad \text{2D surface}$$
$$p_g\left(\frac{\partial h}{\partial x}, \frac{\partial h}{\partial y}\right) = \frac{1}{\sigma_{gx}\sigma_{gy}\ 2\pi}\exp\left[-\frac{(\frac{\partial h}{\partial x})^2}{2\sigma_{gx}^2} - \frac{(\frac{\partial h}{\partial y})^2}{2\sigma_{gy}^2}\right], \quad \text{3D surface} \tag{7}$$

where σ_{gx} and σ_{gy} are the mean surface gradient in the x- and y- directions, which are equal to $\sigma\sqrt{2}/\lambda_x$ and $\sigma\sqrt{2}/\lambda_y$, respectively.

Figure 2 shows three Gaussian surface profiles with different roughness, which are generated using the spectral method (Thorsos, 1988). In this article the Gaussian surface with a Gaussian correlation function is applied, since historically it was the most commonly used model (Thorsos, 1988; Zhang et al., 2011; Eckart, 1953; Ogilvy, 1989). However, the developed elastodynamic theory in the later section, is not restricted to a particular form of the surface statistics.

3. Elastodynamic Kirchhoff theory for the diffuse field

3.1. Kirchhoff assumption

The elastic wave Kirchhoff assumption is illustrated in Fig. (3)(a), where a plane P wave is assumed to be incident on the rough surface. The KA assumes that the motion of one surface point is the same as if it were part of an infinite tangential plane illuminated by the incident wave (Ogilvy, 1991). The total displacement at this point is approximated as a summation of the incident P wave and the reflected P/S waves:

$$\boldsymbol{u}_p = \boldsymbol{d}_0 + r_{pp}\boldsymbol{d}_p + r_{ps}\boldsymbol{d}_s. \tag{8}$$

Here $\boldsymbol{u}_p$ represents the boundary displacement with an incident P wave, r_{pp} and r_{ps} are local reflection coefficients of P and mode converted S waves respectively,

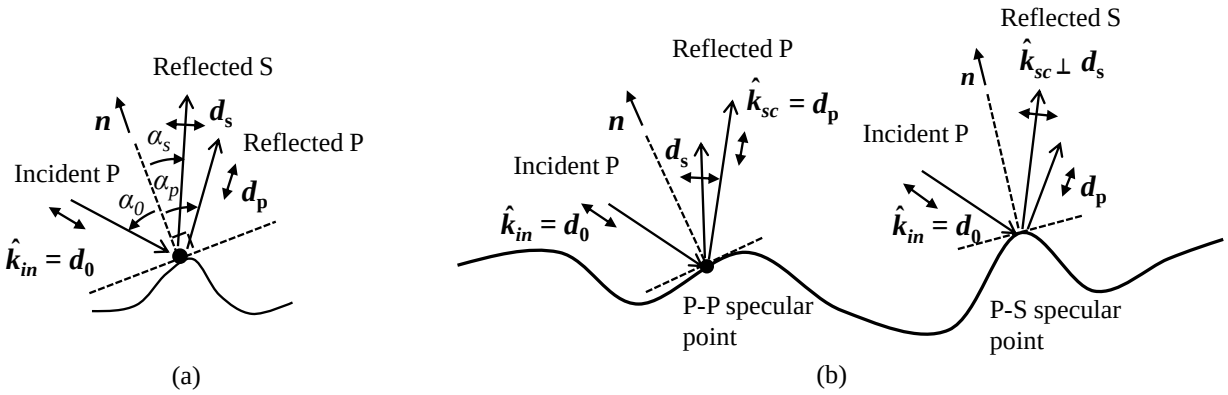

Figure 3: Sketch of the elastodynamic Kirchhoff approximation and the 'specular points'. (a) Tangential plane assumption. (b) 'Specular points' for P-P and P-S modes.

and $\boldsymbol{d}_0$, $\boldsymbol{d}_p$ and $\boldsymbol{d}_s$ are the displacement polarization vectors for the incident P and reflected P/S waves.

According to Snell's law:

$$\alpha_p = \alpha_0, \qquad \frac{\sin\alpha_s}{\sin\alpha_0} = \frac{c_s}{c_p} = \gamma \tag{9}$$

where γ is the ratio of shear-to-compressional wave speed, and α_0, α_p and α_s are local incidence/reflection angles with respect to the normal of the tangential plane. The local reflection coefficients are given by:

$$\begin{aligned} r_{pp} &= \frac{\gamma^2 \sin 2\alpha_0 \sin 2\alpha_s - \cos^2 2\alpha_s}{\gamma^2 \sin 2\alpha_0 \sin 2\alpha_s + \cos^2 2\alpha_s} \\ r_{ps} &= \frac{2\gamma \sin 2\alpha_0 \cos 2\alpha_s}{\gamma^2 \sin 2\alpha_0 \sin 2\alpha_s + \cos^2 2\alpha_s} \end{aligned} \tag{10}$$

3.2. Slope approximations for different wave modes

The elastodynamic Helmholtz integral formula to calculate the scattered displacement, with a stress-free boundary condition (Achenbach, 2003), is:

$$u_k^{sc}(\boldsymbol{R}) = \int_{\mathcal{S}} \Sigma_{ij;k}(|\boldsymbol{R} - \boldsymbol{r}|) u_i(\boldsymbol{r}) n_j(\boldsymbol{r}) d\mathcal{S}(\boldsymbol{r}) \tag{11}$$

where $\Sigma_{ij;k}$ is the stress Green's tensor, u_i is the ith component of the boundary displacement at $\boldsymbol{r}$, n_j is the jth component of the unit normal vector surface pointing towards the observation point at $\boldsymbol{R}$. With a far field approximation that $|\boldsymbol{R}-\boldsymbol{r}| \approx R - \hat{\boldsymbol{R}}\cdot\boldsymbol{r}$, in 3D Eq. (11) can be simplified and converted into the integral along the mean plane of the surface:

$$\boldsymbol{u}^{sc}(\boldsymbol{R}) = -ik_\beta \frac{\exp(ik_\beta r)}{4\pi r}\int_{\mathcal{S}_m} \boldsymbol{U}_{\alpha\beta}\exp(ik_\beta\phi_{\alpha\beta})d\mathcal{S}_m, \quad \alpha,\beta = p,s \tag{12}$$

where $\phi_{\alpha\beta} = A_{\alpha\beta}x + B_{\alpha\beta}y + C_{\alpha\beta}h(x,y)$, and

$$\begin{aligned} A_{\alpha\beta} &= -\frac{k_\alpha}{k_\beta}\sin\theta_{iz}\cos\theta_{ix} - \sin\theta_{sz}\cos\theta_{sx} \\ B_{\alpha\beta} &= -\frac{k_\alpha}{k_\beta}\sin\theta_{iz}\sin\theta_{ix} - \sin\theta_{sz}\sin\theta_{sx} \\ C_{\alpha\beta} &= -\left(\frac{k_\alpha}{k_\beta}\cos\theta_{iz} + \cos\theta_{sz}\right) \end{aligned} \tag{13}$$

The term $\boldsymbol{U}_{\alpha\beta}$ represents the decomposed boundary displacement for different incident/scattering wave modes and is expressed as:

$$\begin{aligned} \boldsymbol{U}_{\alpha p}(\boldsymbol{r},\hat{\boldsymbol{k}}_{\boldsymbol{sc}}) &= \left[(\boldsymbol{u}_\alpha\cdot\boldsymbol{N})\left(1-2\gamma^2\right) + 2\gamma^2(\boldsymbol{u}_\alpha\cdot\hat{\boldsymbol{k}}_{\boldsymbol{sc}})(\boldsymbol{N}\cdot\hat{\boldsymbol{k}}_{\boldsymbol{sc}})\right]\hat{\boldsymbol{k}}_{\boldsymbol{sc}} \\ \boldsymbol{U}_{\alpha s}(\boldsymbol{r},\hat{\boldsymbol{k}}_{\boldsymbol{sc}}) &= (\boldsymbol{N}\cdot\hat{\boldsymbol{k}}_{\boldsymbol{sc}})\boldsymbol{u}_\alpha + (\boldsymbol{u}_\alpha\cdot\hat{\boldsymbol{k}}_{\boldsymbol{sc}})\boldsymbol{N} - 2(\boldsymbol{u}_\alpha\cdot\hat{\boldsymbol{k}}_{\boldsymbol{sc}})(\boldsymbol{N}\cdot\hat{\boldsymbol{k}}_{\boldsymbol{sc}})\hat{\boldsymbol{k}}_{\boldsymbol{sc}} \end{aligned} \tag{14}$$

where $\boldsymbol{N}$ is the unnormalized vector, which equals $(-\partial h/\partial x, -\partial h/\partial y, 1)$. The boundary displacement $\boldsymbol{u}_\alpha$ is obtained using the KA from Eq. (8), which depends on the incident wave mode α. We shall assume an incident P wave, and note that the methodology can be equivalently applied to an incident S wave. In the case of the shear wave, one needs to revise Eq. (8) − (10) according to the representations of a plane S wave reflected from the tangential plane (Ogilvy, 1991).

By examining Eq. (8)∼(10) and Eq. (14), it is immediately noticed that $\boldsymbol{U}_{\alpha\beta}$ is a function involving the incidence/scattering angles and surface slopes, which also rely on the positions of the surface points. It is critical to remove the surface slopes from the integration Eq. (12), to enable the analytical manipulation of the ensemble averaging $< u_k^{sc}\bar{u}_k^{sc} >$. Beckmann's integration by parts, as used for acoustic waves (Ogilvy, 1991), cannot be applied for elastic waves

due to the complicated form of $\boldsymbol{U}_{\alpha\beta}$, and this has halted previous attempts to derive the ensemble averaging.

Instead by noticing that $\boldsymbol{U}_{\alpha\beta}$ is a slowly varying function of position, we apply a stationary phase approach to Eq. (12) to approximate $\boldsymbol{U}_{\alpha\beta}$. The first order derivatives of the phase term $\phi_{\alpha\beta}$ with respect to x and y are both set to be zero to locate the stationary points, and the following expressions are obtained:

$$\frac{\partial h}{\partial x} = -\frac{A_{\alpha\beta}}{C_{\alpha\beta}}, \qquad \frac{\partial h}{\partial y} = -\frac{B_{\alpha\beta}}{C_{\alpha\beta}} \tag{15}$$

Physically Eq. (15) indicates that the slope across the whole surface is approximated as a constant for given incidence/scattering angles and the ratio of the shear-to-compressional wave speed. The approximated slope corresponds to those surface points where the scattering direction is locally viewed to be the same as the specular direction to the incidence angle with respect to the local normal vector $\boldsymbol{n}$. These points are the 'specular points′ originated from the optical Kirchhoff theory (Kodis, 1966), and these elastodynamic 'specular points′ are depicted in Fig. (3)(b) for both P-P and P-S modes. The P-P 'specular points′ are located where the scattering direction coincides with the P wave polarization vector ($\hat{\boldsymbol{k}}_{\boldsymbol{sc}} = \boldsymbol{d}_{\boldsymbol{p}}$), while the P-S 'specular points′ are those where the scattering direction is perpendicular to the S wave polarization vector ($\hat{\boldsymbol{k}}_{\boldsymbol{sc}} \perp \boldsymbol{d}_{\boldsymbol{s}}$). The principal contribution to the integral Eq. (12) is hence made at these 'specular points' corresponding to the stationary points.

By substituting the slope approximation terms in Eq. (15) into Eq. (8) − (10), the expression of the decomposed $\boldsymbol{U}_{\alpha\beta}$ at the 'specular points′ in Eq. (14) is obtained. For comparison with the acoustic and electromagnetic cases (Beckmann and Spizzichino, 1987), we assume that $\boldsymbol{F}_{\alpha\beta}= 1/2\boldsymbol{U}_{\alpha\beta}$. By eliminating the dependence of surface gradient, $\boldsymbol{F}_{\alpha\beta}$ can now be removed from the Kirchhoff integral, and Eq. (12) is simplified to:

$$\boldsymbol{u}^{sc}(\boldsymbol{R}) = -ik_\beta \frac{\exp(ik_\beta r)}{4\pi r} 2\boldsymbol{F}_{\boldsymbol{\alpha\beta}} \int_{\mathcal{S}} \exp(ik_\beta \phi_{\alpha\beta}) d\mathcal{S} \tag{16}$$

where $\boldsymbol{F}_{\alpha\beta}$ is called the elastodynamic angular factor hereinafter, only depending on the incidence/scattering angles and the modes. Note that $\boldsymbol{F}_{\alpha\beta}$ is a vector containing three components due to the polarization of the displacement. Now only terms related with the surface height h are left inside the Kirchhoff integral, and hence the ensemble averaging $< u_k^{sc} \bar{u}_k^{sc} >$ can now be performed analytically.

3.3. Ensemble averaging

The mathematical derivation of the ensemble averaging for elastic waves follows the acoustic case (Ogilvy, 1991). For simplicity we define the scattering intensity as the modulus of the displacement:

$$\begin{aligned} < I_i > &=< u_i^{sc} \bar{u}_i^{sc} >, \quad i = x, y, z \\ < I > &= \sum_{x,y,z} < I_i >, \end{aligned} \tag{17}$$

The expected scattering intensity in 3D is:

$$< I_{i,\alpha\beta} >= \frac{k_\beta^2}{(4\pi r)^2} 4F_{i,\alpha\beta}^2 \int_{\mathcal{S}} \int_{\mathcal{S}} e^{ik_\beta [A_{\alpha\beta}(x_0 - x_1) + B_{\alpha\beta}(y_0 - y_1)]}$$

$$< e^{ik_\beta C_{\alpha\beta}(h_0 - h_1)} > dx_0 dx_1 dy_0 dy_1 \tag{18}$$

By assuming that $\Delta x = x_0 - x_1$ and $\Delta y = y_0 - y_1$, Eq. (18) is simplified via a change of variables:

$$< I_{i,\alpha\beta} >= \frac{k_\beta^2}{(4\pi r)^2} 4F_{i,\alpha\beta}^2 L_x L_y \int_{-\infty}^{\infty} \int_{-\infty}^{\infty} e^{ik_\beta (A_{\alpha\beta}\Delta x + B_{\alpha\beta}\Delta y)}$$

$$\chi_2(k_\beta C_{\alpha\beta}, -k_\beta C_{\alpha\beta}, \Delta x, \Delta y) d\Delta x d\Delta y \tag{19}$$

where $\chi_2(k_\beta C_{\alpha\beta}, -k_\beta C_{\alpha\beta}, \Delta x, \Delta y) = < \exp[ik_\beta C_{\alpha\beta}(h_0 - h_1)] >$, which we call the two-dimensional characteristic function. For a surface following a Gaussian distribution, χ_2 has an analytical form:

$$\chi_2(k_\beta C_{\alpha\beta}, -k_\beta C_{\alpha\beta}, \Delta x, \Delta y) = \exp(-g_{\alpha\beta}[1 - W(\Delta x, \Delta y)]) \tag{20}$$

in which $g_{\alpha\beta} = k_\beta^2 C_{\alpha\beta}^2 \sigma^2$. There is no requirement for a specific form of the correlation function $W(\Delta x, \Delta y)$, except that physically it needs to satisfy the following criteria: (i) W(0,0) = 1; and (ii) W($\Delta x \to \infty$ or $\Delta y \to \infty$) = 0. Eq. (20) is expanded as a Taylor series and substituted into Eq. (19) to obtain the following expression:

$$< I_{i,\alpha\beta} >= \frac{k_\beta^2 F_{i,\alpha\beta}^2 e^{-g_{\alpha\beta}}}{4\pi^2 r^2} L_x L_y \Sigma_{n=0}^{\infty} \frac{g_{\alpha\beta}^n}{n!}$$

$$\int_{-\infty}^{\infty}\int_{-\infty}^{\infty} e^{ik_\beta(A_{\alpha\beta}\Delta x + B_{\alpha\beta}\Delta y)} W^n(\Delta x, \Delta y) d\Delta x d\Delta y \tag{21}$$

Substituting the Gaussian correlation function Eq. (6) into Eq. (21) yields a separation of the total intensity into its coherent and diffuse components:

$$\begin{aligned} &< I_{i,\alpha\beta} >= I_{i,\alpha\beta}^c + I_{i,\alpha\beta}^d \\ &I_{i,\alpha\beta}^c = I_i^{fs} e^{-g_{\alpha\beta}}, && \text{coherent} \\ &I_{i,\alpha\beta}^d = \frac{k_\beta^2 F_{i,\alpha\beta}^2 \lambda_x \lambda_y e^{-g_{\alpha\beta}}}{4\pi r^2} L_x L_y \Sigma_{n=1}^{\infty} \frac{g_{\alpha\beta}^n}{n! n} \exp\left[-\frac{k_\beta^2 (A_{\alpha\beta}^2 \lambda_x^2 + B_{\alpha\beta}^2 \lambda_y^2))}{4n}\right] && \text{diffuse} \end{aligned} \tag{22}$$

In 2D the coherent intensity has the same form as that in 3D, but the diffuse intensity needs to be revised as:

$$< I_{i,\alpha\beta}^d >= \frac{k_\beta F_{i,\alpha\beta}^2 \lambda_x \sqrt{\pi} e^{-g_{\alpha\beta}}}{2\pi r} L_x \Sigma_{n=1}^{\infty} \frac{g_{\alpha\beta}^n}{n! \sqrt{n}} \exp\left[-\frac{k_\beta A_{\alpha\beta}^2 \lambda_x^2}{4n}\right] \tag{23}$$

By examining Eq. (22) and Eq. (23), the mode coupling for the diffuse field is embedded in the angular factor $F_{i,\alpha\beta}$, the decay factor $g_{\alpha\beta}$, and the exponential term inside the finite summation.

3.4. Asymptotic solutions

The diffuse field is dominant when the roughness or the frequency is high. By passing the Kirchhoff integral to the high frequency limit that $k_\beta C_{\alpha\beta}(h_0 - h_1) \approx k_\beta C_{\alpha\beta}(\frac{\partial h}{\partial x}\Delta x + \frac{\partial h}{\partial y}\Delta y)$ when $k_\beta \to \infty$, the diffuse field can be approximated as:

$$
\begin{aligned}
< I_{i,\alpha\beta} > &= \frac{k_\beta^2 F_{i,\alpha\beta}^2}{4\pi^2 r^2} L_x L_y \int_{-\infty}^{\infty}\int_{-\infty}^{\infty} < e^{ik_\beta[(A_{\alpha\beta}+C_{\alpha\beta}\frac{\partial h}{\partial x})\Delta x+(B_{\alpha\beta}+C_{\alpha\beta}\frac{\partial h}{\partial y})\Delta y]} > d\Delta x d\Delta y \\
&= \frac{k_\beta^2 F_{i,\alpha\beta}^2}{4\pi^2 r^2} L_x L_y \times \frac{(2\pi)^2}{k_\beta^2 C_{\alpha\beta}^2} < \delta\left(\frac{\partial h}{\partial x}+\frac{A_{\alpha\beta}}{C_{\alpha\beta}}, \frac{\partial h}{\partial y}+\frac{B_{\alpha\beta}}{C_{\alpha\beta}}\right) > \\
&= \frac{F_{i,\alpha\beta}^2}{r^2 C_{\alpha\beta}^2} L_x L_y \int_{-\infty}^{\infty}\int_{-\infty}^{\infty} p_g(\gamma_x,\gamma_y) d\gamma_x d\gamma_y \delta\left(\gamma_x+\frac{A_{\alpha\beta}}{C_{\alpha\beta}}, \gamma_y+\frac{B_{\alpha\beta}}{C_{\alpha\beta}}\right) \\
&= \frac{F_{i,\alpha\beta}^2}{r^2 C_{\alpha\beta}^2} L_x L_y \times p_g\left(\frac{\partial h}{\partial x}=-\frac{A_{\alpha\beta}}{C_{\alpha\beta}}, \frac{\partial h}{\partial y}=-\frac{B_{\alpha\beta}}{C_{\alpha\beta}}\right)
\end{aligned}
\tag{24}
$$

In 2D, a similar equation is found to be:

$$
< I_{i,\alpha\beta} >= \frac{F_{i,\alpha\beta}^2}{r C_{\alpha\beta}} L_x \times p_g\left(\frac{\partial h}{\partial x}=-\frac{A_{\alpha\beta}}{C_{\alpha\beta}}\right) \tag{25}
$$

where p_g is the distribution for the surface slopes shown in Eq. (7). In the high frequency limit the scattering intensity is proportional to the angular factor, and the pdf of the surface slopes, only at the 'specular points′. Contributions from 'non-specular points′ vanish rapidly due to fast oscillation of the phase, and hence have almost no effects on the Kirchhoff integral. The total intensity is equivalent to the dominant diffuse intensity. In contrast, when the roughness is small a low frequency approximation is obtained from Eq. (22) in 3D or Eq. (23) in 2D by only keeping the first few terms. The number of terms for the convergence depends on both the RMS and the correlation length. Generally it is found that keeping the first four terms is sufficient for the convergence when $\sigma \leq \lambda_p/8$. Note that the high frequency asymptotic solution does not require any restriction on the pdf of the height or the height gradient.

4. Monte Carlo verification

Monte Carlo simulations are run using Gaussian surfaces from low to high roughness to assess the accuracy of the developed elastodynamic theory. For each realization of the surface profile, the Kirchhoff integral in Eq. (12) is performed numerically without the slope approximation, and a sample mean of the total intensity is obtained from 500 realizations of surfaces for each roughness.

A more rigorous way is to apply the purely numerical method implemented in Shi et al. (2015) instead of the Kirchhoff model as a benchmark. However, the validity of the Kirchhoff approximation has been carefully evaluated by comparison with the numerical method in both 2D and 3D (Zhang et al., 2011; Shi et al., 2015) . Hence for the roughness values considered in this article ($\sigma \leq \lambda_p/3, \lambda_x \geq \lambda_p/2$), the choice of either methods would lead to the same conclusion since the KA is within its range of validity. The bulk medium is chosen to be Aluminium with Young's modulus of 70GPa, density of 2700kg/m^3 and Poisson's ratio of 0.33. The S-to-P wave speed ratio γ is therefore approximately 0.5 with $c_p = 6198$m/s, and $c_s = 3122$m/s. The incident wave on the surface is assumed to be a 4MHz monochromatic plane P wave, and the corresponding wavelengths for P and S modes are 1.54mm and 0.77mm.

4.1. Simulation using 2D surfaces

In 2D the length of the surface is 6mm ($\approx 4\lambda_p$) and the roughness parameters are $\sigma = \lambda_p/10$ to $\lambda_p/3$, and $\lambda_x = \lambda_p/2$. A modest incidence angle θ_i of 30^o is assumed when the mode conversion is strong. Figure 4 shows the comparison of the expected scattering pattern for different modes predicted from the analytical Kirchhoff formulae and the benchmark Monte Carlo simulations. The high frequency asymptotic solution calculated from Eq. (25), and the low frequency approximation from Eq. (22) and (23) with the first four terms are both plotted as well. The quantities for comparison are $< I_{z,pp} >$ for the P-P mode and $< I_{x,ps} >$ for the P-S mode, defined in Eq. (17) as the z- and x-components of the scattering intensity. The values of the intensities have been normalized by the normal pulse echo response for the P-P mode from a flat surface with the same dimension. As can be seen, the theoretical results show excellent agreement with the numerical results from Monte Carlo simulations, and the agreement is found from low ($\sigma = \lambda_p/10$) to high roughness ($\sigma = \lambda_p/3$). In addition, the low and high frequency asymptotic solutions are both very accurate as well.

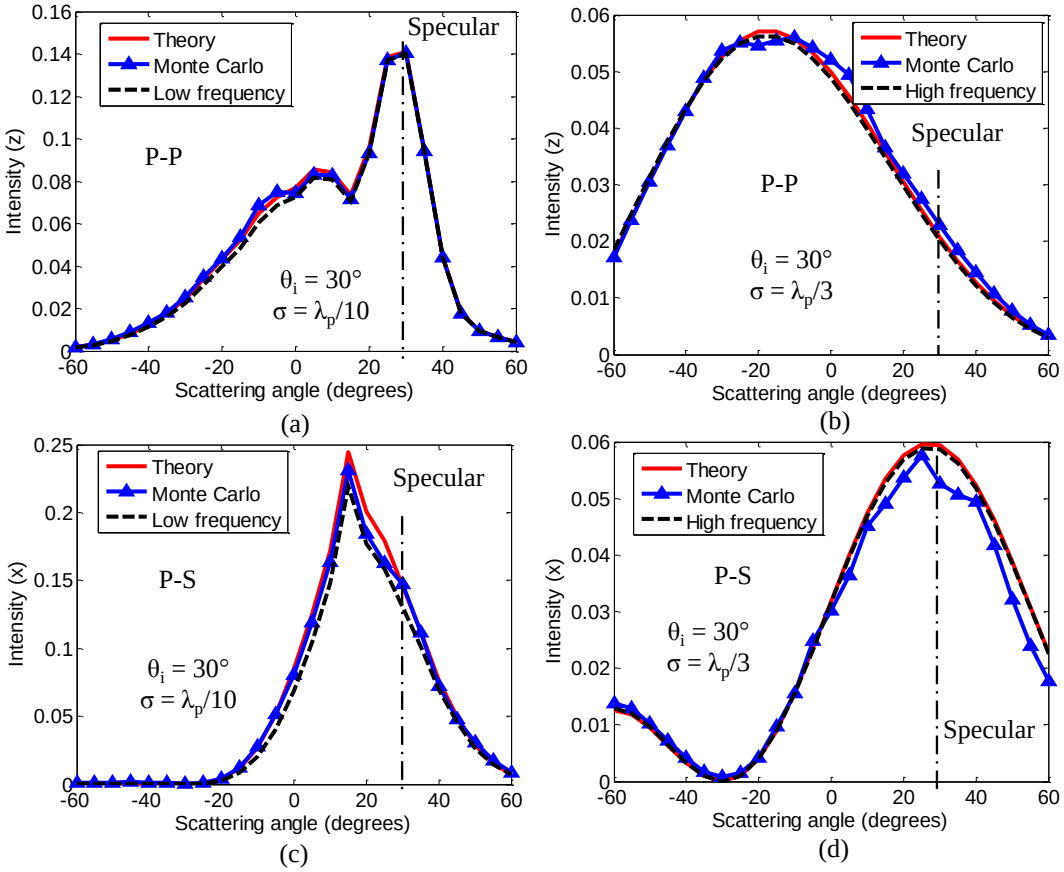

Figure 4: 2D scattering patterns obtained from the elastodynamic theory, Monte Carlo simulations and high/low frequency solutions, with an oblique incidence angle of 30^o. (a) P-P mode, $\sigma = \lambda_p/10$, $\lambda_x = \lambda_p/2$. (b) P-P mode, $\sigma = \lambda_p/3$, $\lambda_x = \lambda_p/2$. (c) P-S mode, $\sigma = \lambda_p/10$, $\lambda_x = \lambda_p/2$. (d) P-S mode, $\sigma = \lambda_p/3$, $\lambda_x = \lambda_p/2$.

It is noticeable that in Fig. 4(a), there is a sharp peak at the specular direction ($\theta_s = 30^o$) for the P-P mode, contributed from the dominant coherent components. As the roughness increases to $\sigma = \lambda_p/3$, a clear peak is observed around the backward angle instead (θ_s = -30^o) in Fig. 4(b). Note that the backscattering peak is not as concentrated as the specular peak shown in Fig. 4(a) because it is formed by the dominant diffuse field, whose energy is more widely distributed. Furthermore, as noticed in Fig. 4(d), at high roughness

the scattered S waves show a dipole-like pattern, with the peak located around the specular angle and the valley at the backward angle. A detailed physical analysis regarding the mode conversion is provided in the last section of this article.

4.2. Simulation using 3D surfaces

The elastodynamic theory is also evaluated on 3D Gaussian surfaces with the same bulk medium as the 2D cases. The surface has a dimension of 6×6 mm^2 ($\approx 4\lambda_p \times \lambda_p$), with $\sigma = \lambda_p/10$ to $\lambda_p/4$, and $\lambda_x = \lambda_y = \lambda_p/2$. The incident P wave is within the x-z plane with an angle of 30^o ($\theta_{ix} = 180^o$, $\theta_{iz} = 30^o$). By changing θ_{sx} from 0^o to 360^o and θ_{sz} from 0^o to 60^o, the entire 3D scattering pattern can be obtained.

Figure. 5 and 6 show the comparison of the scattering patterns between the elastodynamic theory (first row), and the sample mean from the Monte Carlo simulations (second row) for different wave modes, from low to high roughness. The scattering patterns are plotted as a function of the unit scattering vectors $\hat{k}_{sx}$ and $\hat{k}_{sy}$ defined in Eq. (2). It is equivalent to an angular projection of the scattering field into the x-y plane viewed from the z direction. The pixels represent the value of the scattering intensity, which are again normalized by that of a normal pulse echo response from a flat 3D surface with the same dimension. Three intensities are shown here, with $< I_{z,p-p} >, < I_{x,p-sv} >$ and $< I_{y,p-sh} >$ plotted for P-P, P-SV and P-SH mode, respectively. Good agreement between the theory and the Monte Carlo simulations is found for all modes from low to high roughness.

The coherent peaks can be found around the specular directions for both P-P and P-SV modes in Fig. 5(a) and (b). When the roughness increases, a more widely spread peak around the backward angle is seen for the P-P mode in Fig. 6(a), due to the diffuse field and the mode conversion similar with the

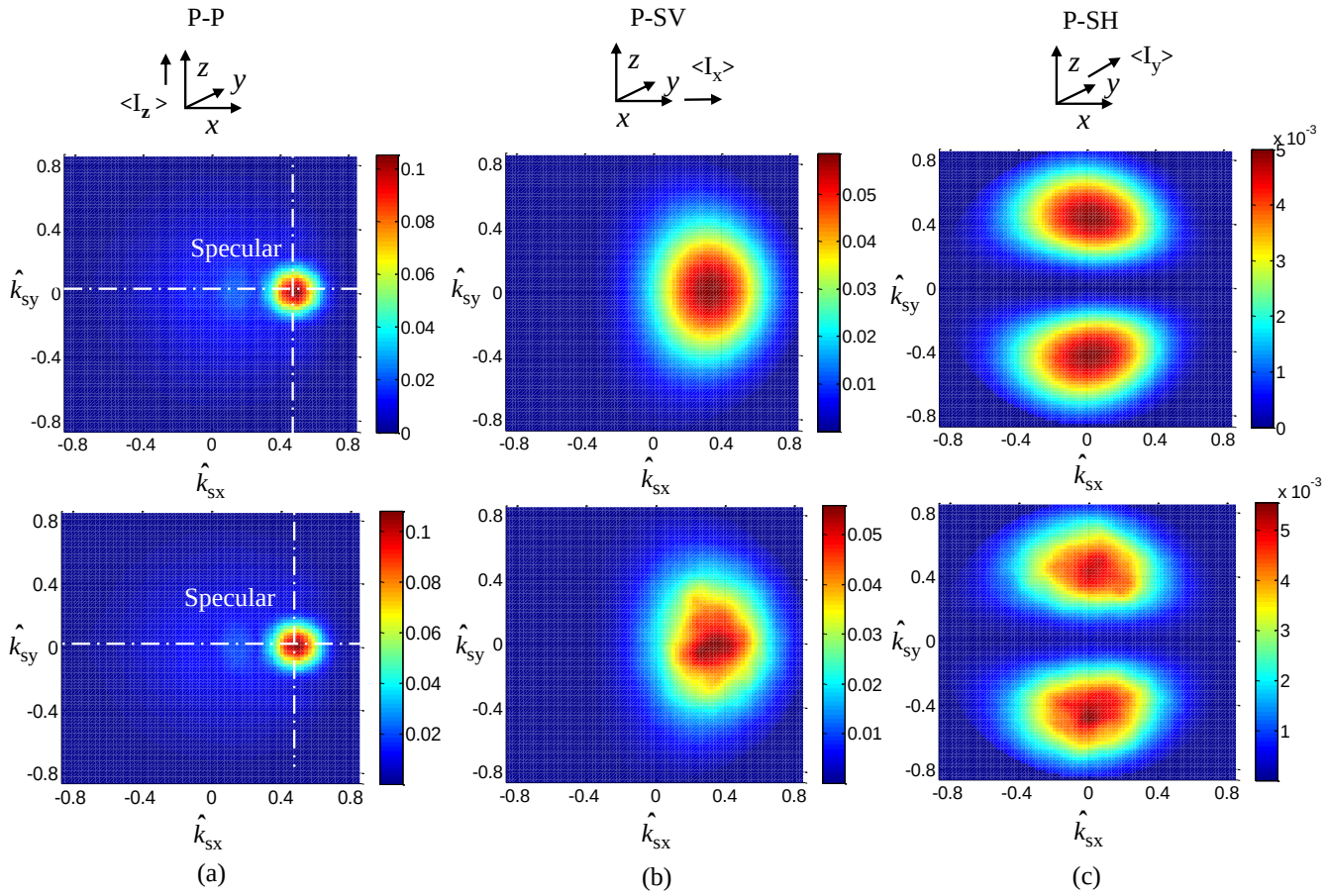

Figure 5: 3D scattering patterns obtained from the elastodynamic theory and the Monte Carlo simulations for cases of low roughness, when $\sigma = \lambda_p/10$ and $\lambda_x = \lambda_y = \lambda_p/2$, with a modest incidence angle ($\theta_{iz} = 30^o, \theta_{ix} = 180^o$). (a) P-P mode. (b) P-SV mode. (c) P-SH mode. (Plots in the first row represent the ensemble average from the theory; Plots in the second row represent the sample average from Monte Carlo simulations)

2D plots shown in Fig. 4(b). Furthermore, the scattering pattern for the SH mode is symmetric about the plane of the incidence wave for both low and high roughness as noticed in Fig. 5(c) and Fig. 6(c), which is mainly due to the isotropic nature of the surface.

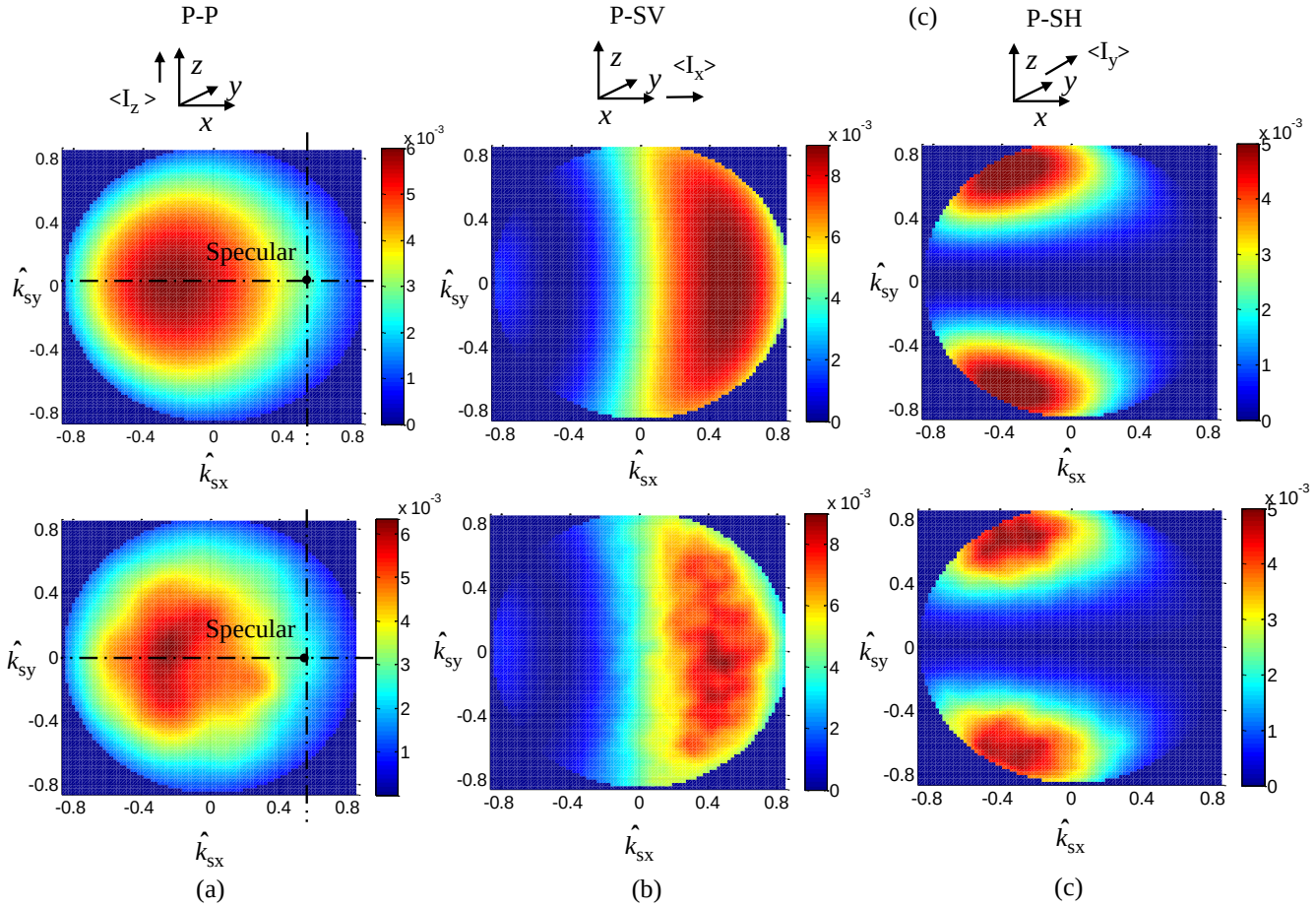

Figure 6: 3D scattering pattern obtained from the elastic theory and the Monte Carlo simulations for cases of high roughness, when $\sigma = \lambda_p/4$ and $\lambda_x = \lambda_y = \lambda_p/2$, with a modest incidence angle ($\theta_{iz} = 30^o, \theta_{ix} = 180^o$). (a) P-P mode. (b) P-SV mode. (c) P-SH mode. (Plots in the first row represent the ensemble average from the theory; Plots in the second row represent the sample average from Monte Carlo simulations)

5. Experimental validation

To yet further validate the elastodynamic theory an experiment with two ultrasonic phased arrays is performed, which is illustrated in Fig. 7(a). A rough surface is manufactured on the bottom of an Aluminum block ($260\times80\times60\text{mm}^3$), and it is corrugated so that the height remains invariant in the y- direction

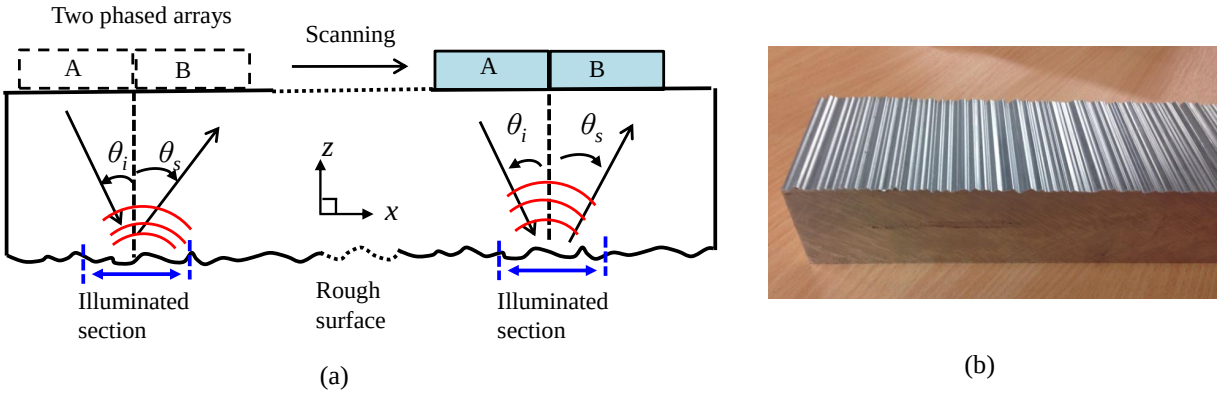

Figure 7: Experimental setup. (a) Illustration of the experimental methodology. (b) Picture of the sample (Length: 260mm; Width: 80mm; Height: 60mm).

shown in Fig. 7(b). The surface is made by a CNC (computer numerical control) milling machine using a drilling cutter, and follows a profile generated by a Gaussian distribution of heights. Two 2D linear phased arrays both with 32 elements are placed tightly together on the top flat surface of the sample, and the parameters of the phased array are given in Table 1. In practice, elements numbered from 7 to 14 of array A are fired to produce the P wave with an incidence angle of 30^o using a time delay law to steer a columnated beam in the chosen direction; in total all the 64 elements are used for receiving the scattered waves, corresponding to different angles. The input signal is assumed to be a five-cycle tone burst with a centre frequency of 2MHz, and hence the P wavelength is 3.1mm. The RMS and the correlation length of the corrugated surface are 0.75mm ($\lambda_p/4$) and 1.54mm ($\lambda_p/2$) respectively. Note that the minimum dimension of the drilling cutter is 2mm, which might somewhat reduce the accuracy of the manufactured shapes of some 'peaks' and 'valleys' of the surface. However, this would not affect the main conclusion which will be shown later.

To acquire multiple realizations of the illuminated surfaces, the phased arrays are moved, or scanned across the top flat surface with a spatial interval

Number of elements per array	32
Element width	20mm
Inter elements pitch	1.6mm
Inter elements space	0.25mm
Centre frequency	2MHz
Bandwidth (-6dB)	1.3MHz

Table 1: Parameters of the ultrasonic phased array

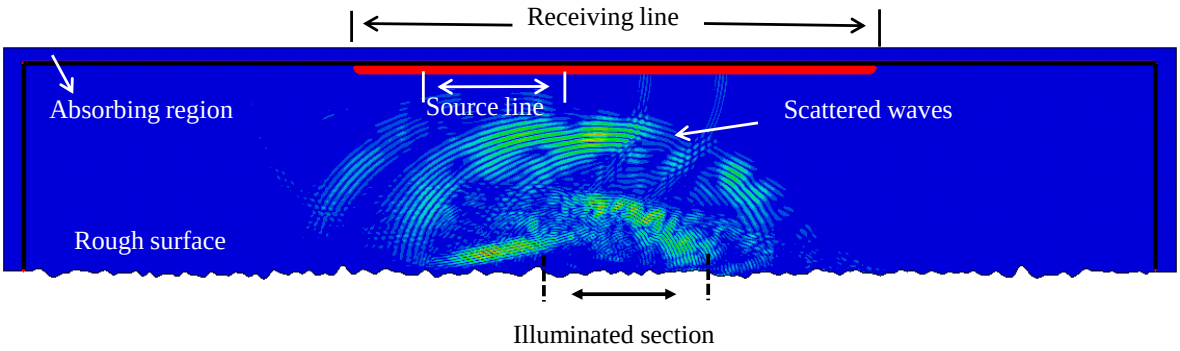

Figure 8: Snapshot of animation in the FE simulation showing the waves scattered from the sample corrugated rough surface.

of 8mm. In this manner, scattering from 16 different surfaces with the same statistics are obtained, and the displacements (u_z) are recorded in each scan. By transferring the received signals into the frequency domain and extracting the amplitude at the centre frequency, the scattering amplitude and hence the intensity is obtained for each realization/scan. The expected value of the scattering intensity is approximated by an arithmetic average from all scans.

5.1. Numerical simulation of the experiment

The experiment is first numerically simulated using a finite element (FE) model with Abaqus (Dassault Systemes Simulia Corp., Providence, RI). The

purpose of the numerical simulation is to test the feasibility of the experimental methodology and gain more confidence before conducting the real experiment. The simulation is performed in 2D as the surface height is invariant in the y- direction. Figure 8 shows the animation for waves scattered from the sample surface for one scan. The FE model has a dimension of 259×66mm^2 ($\approx 168\lambda_p \times 43\lambda_p$), including the absorbing region with a thickness of 4.5mm ($\approx 3\lambda_p$) (Rajagopal et al., 2012). According to the geometry of the sample and the parameters of the phase arrays, the lengths of the source line and the receiving line are 12.75mm ($\approx 8\lambda_p$) and 113mm ($\approx 73\lambda_p$), respectively. The scanning with phased arrays is simulated by selecting different nodes representing the source and the receiving line. After running multiple FE simulations, the scattered P waves are simply separated from the S waves from the received time traces using a time window. As seen in Fig. 7(a), the propagation distances r of the scattered waves from the illuminated surface to array elements vary, corresponding to different spatial decay factors $1/\sqrt{r}$ in 2D. To account for this spatial attenuation, the obtained scattering intensity at each angle needs to be normalized by a factor of $\cos\theta_s$.

The sample averaged scattering intensity from 16 scans using the FE simulation is plotted in Fig. 9, in comparison with that predicted from the elastodynamic theory; the FE results have a reassuring match with the shape of the theoretical curve. A peak is seen when the scattering angle is around -20^o due to the dominant diffuse field at such a high roughness. The variations of the FE raw data are caused by the limited number of realizations used for averaging in the simulation. Running more FE simulations would reduce the variations and in the end converge. However, a best fit of the simulated FE raw data from 16 scans using a polynomial up to the 3rd-order gives a smooth curve, which shows very good agreement with the theoretical curve.

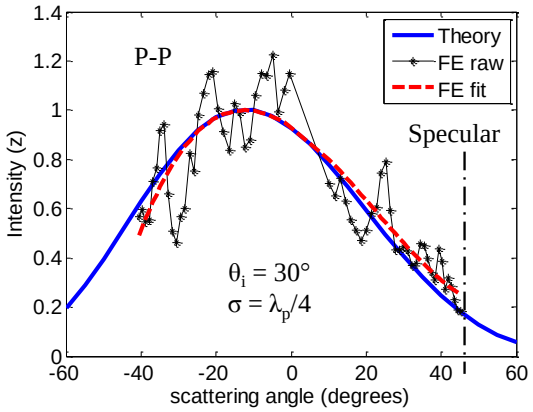

Figure 9: Comparison of the scattering pattern between the theory and the simulation, for a P wave with an angle of 30^o incident on a corrugated surface with the RMS of 0.75mm ($\lambda_p/4$) and the correlation length of 1.54mm ($\lambda_p/2$).

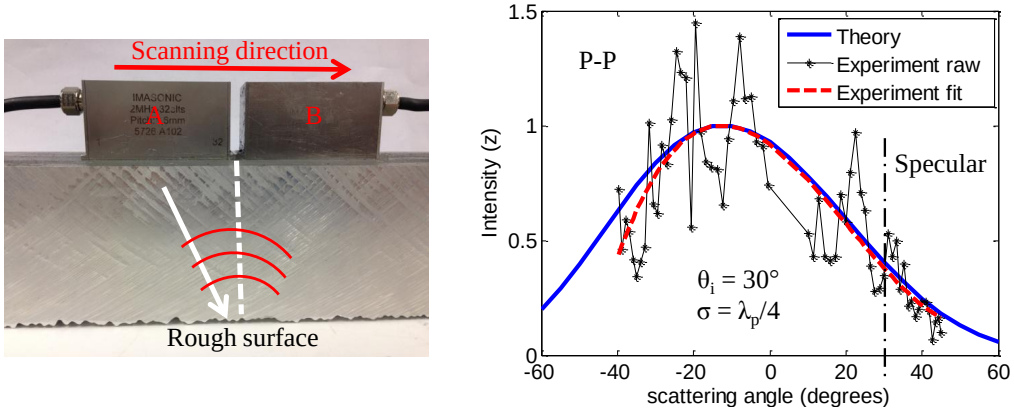

Figure 10: Experiment and the results. (a) Picture of the experiment with two phased arrays. (b) Comparison of the scattering pattern between the theory and the experiment, for a P wave with an angle of 30^o incident on a corrugated surface with the RMS of 0.75mm ($\lambda_p/4$) and the correlation length of 1.54mm ($\lambda_p/2$).

5.2. Experimental results

After the numerical simulation, the experiment using two phased arrays (Imasonic, Besancon, France) is performed, shown in Fig. 10(a), in the same scanning manner as the FE simulation. Apart from the spatial attenuation factor $\cos\theta_s$ to account for different propagation distances from the illuminated surface to array elements, in a real experiment the measured scattering intensity at each angle needs to be further scaled by a directivity factor (Drinkwater and Wilcox, 2006). The averaged scattering pattern, denoted as the experiment raw data, from multiple scans, is shown in Fig. 10(b) along with the theoretical curve. As can be seen the experimental raw data follows the shape of the theoretical solution, although large variations are seen. A best fit using a 3rd-order polynomial is applied on the measured data to compensate for the limited number of scans, and a very good match can now be found between the theory and the experiment.

Note that the theoretical formulae are derived from the assumption of an ideal plane wave scattering in the far field. To avoid the difference caused by a finite beam in the simulation and the experiment, the scattering intensity is normalized by the peak of the fitted data. A more rigorous comparison would need to incorporate the beam model into Eq. (22) and (23) to revise the theoretical formulae to represent the expected intensity, but this is not pursued here. However, the agreement of the shape of the patterns is clearly demonstrated in Fig. 9 and 10(b) between the experiment, FE simulation and the theory.

6. Physical discussion on the mode conversion

To gain a thorough understanding of the mode conversion of elastic waves influenced by the surface roughness, in this section the developed theory is utilized to analyze the effect of roughness on the elastic wave scattering intensity, with focus on the scattering into P and mode converted S waves. In addition, the

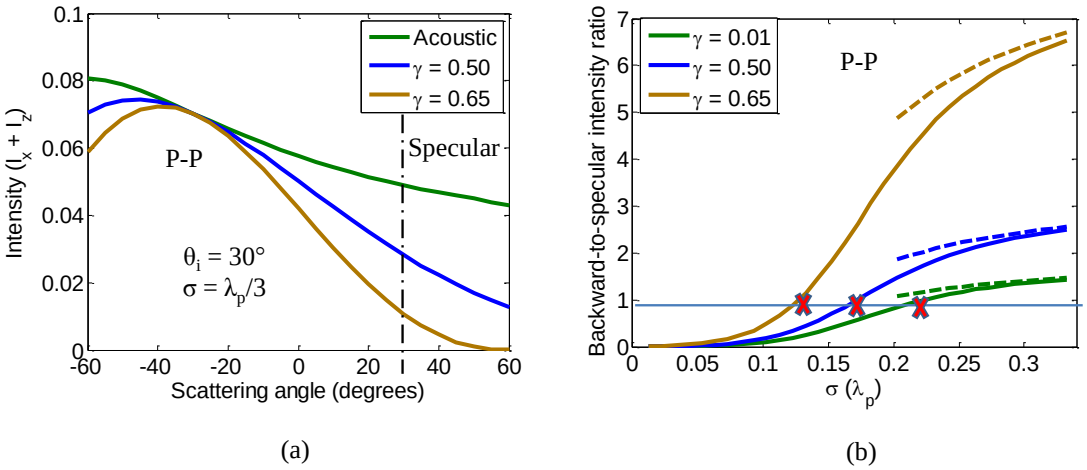

Figure 11: Scattering intensity for the P-P mode with an oblique incidence angle of 30^o. (a) Scattering patterns when $\sigma = \lambda_p/3$. (b) Backward-to-specular intensity ratio for the P-P mode as a function of σ. (The dashed lines denote the high frequency asymptotic solutions.)

appearance of the SH mode and its depolarization caused by the 3D roughness are also investigated.

6.1. P-P mode

The P-P scattering patterns of $< I_{pp} >$ with different S-to-P wave speed ratio γ when $\sigma = \lambda_p/3$ are shown in Fig. 11(a), along with the acoustic intensity when no mode conversion occurs. The intensity plotted here is the summation of its components in both x- and z- directions. The backscattering intensity is much larger than the specular intensity at such a high roughness, when the diffuse field is dominant. The elastic and the acoustic intensities coincide at the backscattering angle, and start to diverge as the scattering angle is away from the backward direction due to the mode conversion. The specular intensity is decaying quickly as γ increases, which results in a clearer peak around the backward angle for the elastic wave. The peak would become more pronounced if plotting only the z- directional scattering intensity $< I_{z,pp} >$ as shown in Fig. 4(b), which is the actual quantity that is measured in a real inspection.

In contrast, the acoustic intensity has no peak since it is almost isotropically distributed. Hence the appearance of the backscattering peak is caused by both the diffuse field and the elasticity, which includes the mode conversion and the displacement polarization.

In Fig. 11(b) the backward-to-specular intensity ratio for the P-P mode is shown as a function of the RMS value. The dashed line denotes the high frequency asymptotic solutions from Eq. (25). Apparently the ratio is increasing quickly as the surface appears to be more rough, and it is also relatively larger when the S-to-P wave speed ratio increases. By setting $\theta_s = -\theta_i$ or $\theta_s = \theta_i$ in Eq. (25), the 2D backward/specular intensity and the relative ratio with a high roughness is expressed as:

$$
\begin{aligned}
&< I_{pp}(\theta_s = -\theta_i) >= \frac{L_x}{2\sqrt{2\pi}\cos^3\theta_i r} \cdot \frac{1}{\sigma_g} \exp\left[-\frac{\tan^2\theta_i}{2\sigma_g^2}\right], \quad \text{Backward intensity} \\
&< I_{pp}(\theta_s = \theta_i) >= \frac{L_x F_{pp}^2(\theta_s = \theta_i)}{2\sqrt{2\pi}\cos\theta_i r} \cdot \frac{1}{\sigma_g}, \qquad \text{Specular intensity} \\
&\frac{< I_{pp}(\theta_s = -\theta_i) >}{< I_{pp}(\theta_s = \theta_i) >} = \frac{\exp[-\frac{\tan^2\theta_i}{2\sigma_g^2}]}{\cos^2\theta_i F_{pp}^2(\theta_s = \theta_i)}
\end{aligned}
\tag{26}
$$

Recall that the RMS gradient $\sigma_g = \sqrt{2}\sigma/\lambda_0$, and in the high frequency limit the intensity should be only related to the surface gradient as shown in Eq. (25). Clearly the backward intensity is a function only of roughness, showing the same value for any S-to-P wave speed ratio, including the extreme acoustic case. This is not surprising since for any stress-free flaw in an isotropic elastic solid the Kirchhoff approximation for the pulse-echo far-field scattering amplitude is identical to the Kirchhoff approximation for the scalar scattering amplitude of a void in a fluid (Schmerr and Song, 2007). Hence the specific observation of the lines meeting at the backward angle in Fig. 11(a) can be generalized to other values of roughness. However, the specular intensity does not only rely on the roughness σ_g, but also on the mode conversion through $F_{pp}(\theta_i = \theta_s)$, as part of the incident P waves are converted to S waves. Note that for the P-P mode the effects from the mode conversion and the roughness

are decoupled. Specifically, the mode conversion is only included in the angular factor $F_{pp}(\theta_s = \theta_i)$, and the effect of the roughness is shown in σ_g. Furthermore, From Eq. (26) it is easy to find that the backward-to-specular intensity ratio increases as the roughness increases, as shown in Fig. 11(b).

It might be interesting to calculate the roughness value when the backward and the specular intensity is equivalent, marked as the intersection points in Fig. 11(b). To estimate the corresponding σ, the full solution Eq. (22) is used and we let the backward and the specular intensity be equal, by keeping the first four terms. The resulting equation has only one unknown variable σ, which is then solved numerically. For example, in this way the RMS value σ when $\gamma = 0.5$ is calculated approximately as $0.17\lambda_p$.

6.2. P-S mode

To further illustrate the effects of the roughness and the elasticity on mode converted S waves, Fig. 12(a) shows the dipole-like scattering patterns for the P-S mode with different S-to-P wave speed ratio when $\sigma = \lambda_p/3$; at the backward direction the S wave intensity vanishes as expected, and it reaches a peak around the specular angle, indicating a strong mode conversion effect. It needs to be mentioned that in (Shi et al., 2015) the valid region of the Kirchhoff approximation was established only for the P-P mode. Hence for the roughness shown here ($\sigma = \lambda_p/3 = \lambda_s/1.5$), we cannot be as confident about the accuracy of the scattering intensity for the P-S mode as for the P-P mode, since the scattered S wave shows a shorter wavelength. However, the trend of the scattering pattern for the P-S mode should remain the same as the roughness is not extremely high.

In Fig. 12(b) the coherent and the diffuse intensity in the specular direction ($\theta_s = 30^o$) are plotted separately for both P-P and P-S modes. Again the dashed lines represent the low frequency approximation by keeping the first four terms in Eq. (23) and the high frequency asymptotic solution, which connect well around $\sigma = \lambda_p/8$ to give the intensity covering the entire frequency range.

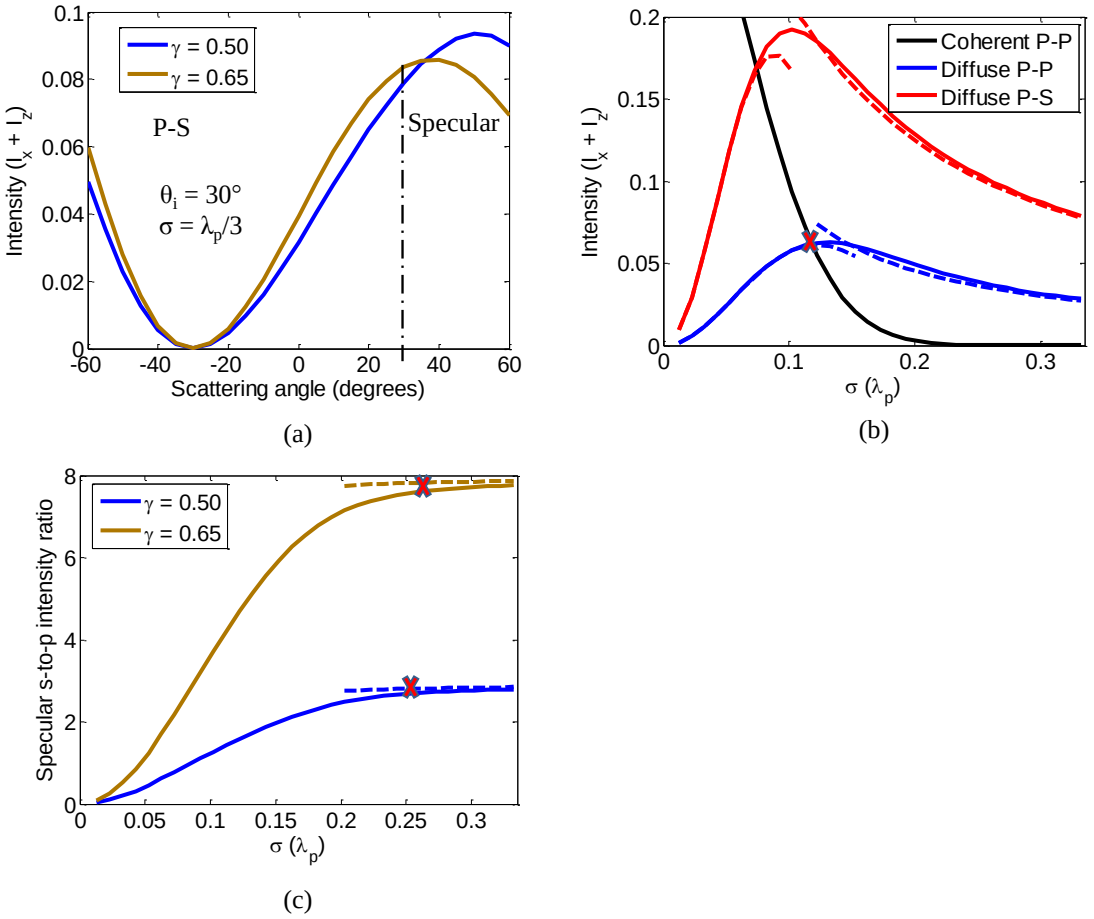

Figure 12: Mode converted S waves with an oblique incidence angle of 30^o. (a) Scattering patterns for the P-S mode when $\sigma = \lambda_p/3$. (b) Coherent and diffuse intensities for P-P and P-S modes in the specular direction. (c) Specular S-to-P intensity ratio as a function of σ. (The dashed lines represent the solutions from low and high frequency approximations)

Apparently the diffuse intensity for the mode converted S waves is much larger than for the P waves, which implies a significant energy leakage from the incident P to scattered S waves.

425

To quantify the mode conversion effect, the Specular S-to-P intensity ratio is shown in Fig. 12(c) with respect to the RMS value σ. It is seen that the

mode conversion effect increases when the surface becomes more rough in the specular angle, and levels off approximately after $\sigma = \lambda_p/4$. By using Eq. (25), the high frequency asymptotic solution for the P-S mode scattering intensity in the specular angle is expressed as:

$$< I_{ps}(\theta_s = \theta_i) >= \frac{F_{ps}^2 L_x}{(\gamma+1)\sqrt{2\pi}\cos\theta_i r\sigma_g} \exp\left[-(\frac{\gamma-1}{\gamma+1})^2 \frac{\tan^2\theta_i}{2\sigma_g^2}\right] \tag{27}$$

In Eq. (27), for the P-S mode the effects of the roughness and the mode conversion are no longer decoupled, which is different from the P-P mode case shown in Eq. (26). The Specular S-to-P intensity ratio can hence be expressed as:

$$\frac{< I_{ps}(\theta_s = \theta_i) >}{< I_{pp}(\theta_s = \theta_i) >} = \frac{F_{ps}^2}{F_{pp}^2} \frac{2}{\gamma+1} \exp\left[-(\frac{\gamma-1}{\gamma+1})^2 \frac{\tan\theta_i^2}{2\sigma_g^2}\right] \tag{28}$$

When pushing Eq. (28) to the extreme high frequency limit by assuming that $\sigma_g \to \infty$, Eq. (28) is simplified to:

$$\frac{< I_{ps}(\theta_s = \theta_i) >}{< I_{pp}(\theta_s = \theta_i) >} = \frac{F_{ps}^2}{F_{pp}^2} \frac{2}{\gamma+1} \tag{29}$$

which only depends on the incidence angle and the S-to-P wave speed ratio. Using Eq. (29), the value of the plateau in the high frequency for the S-to-P intensity ratio can be predicted. For instance, by substituting $\gamma = 0.50$ and 0.65 into Eq. (29), the S-to-P intensity ratio is calculated as 2.91 and 7.93 as marked in Fig. 12(c), showing very good agreement with the curves.

In addition, from Fig. 12(b) a noticeable peak is seen at an intermediate roughness ($\sigma \approx \lambda_p/8$) for both diffuse P-P and P-S intensity, and for the P-P mode it almost coincides with the intersection point when the coherent and the diffuse intensities are equivalent, as marked by the red cross in the plot. Small roughness ($\sigma \leq \lambda_p/8$) causes the appearance of the diffuse field, which then starts to be attenuated by increased roughness after σ is larger than some intermediate value σ_{med}. Hence σ_{med} is some measure of the roughness of the surface, indicating whether the roughness constructively or destructively affects the diffuse intensity. According to Eq. (23), the value of σ_{med} is found by letting

$\frac{\partial I_{pp}^d}{\partial \sigma} = 0$ and solving the resulting equation:

$$\sum_{n=1}^{\infty} \frac{(n-g)g^{n-1}}{n!\sqrt{n}} = 0 \tag{30}$$

Where $g = 4k_p^2\sigma^2\cos^2\theta_i$. By keeping the first four terms of Eq. (23), the value of σ is found as $\lambda_p/7.5$.

To better understand the intermediate RMS value around $\lambda_p/7.5$, the Rayleigh parameter is quoted here (Ogilvy, 1991):

$$R_a = k_p\sigma\cos\theta_i \tag{31}$$

It represents the averaged relative phase difference of scattered waves from two surface points in the specular direction. The Rayleigh criterion states that if $R_a \leq \pi/4$, then the surface is 'smooth', otherwise it is 'rough'. By substituting θ_i =30^o into Eq. (31), the critical σ is calculated as $\lambda_p/7$, which is almost the same as the value solved from Eq. (30) corresponding to the peak of the diffuse intensity. Therefore the critical RMS from the conventional Rayleigh criterion agrees with the RMS for the peak point of the diffuse intensity, and also the intersection point of the coherent and the diffuse intensity.

6.3. 3D roughness induced SH mode and depolarization

For an elastic wave scattered from a smooth surface or a corrugated surface infinitely long in the y- direction, the displacement polarization is within the x-z plane, often called the in-plane motion. If the surface is rough as a function of both x and y, the in-plane waves are coupled with the shear horizontal (SH) waves in the x-y plane. The 'depolarization$'$ occurs, as the displacement is now composed of both in-plane and out-of-plane motions induced by the roughness in the y-axis.

In this section, a study is performed to analyze the depolarization effect for the SH mode using the developed formulae. Specifically, the quantity $I_{y,ps}$ is

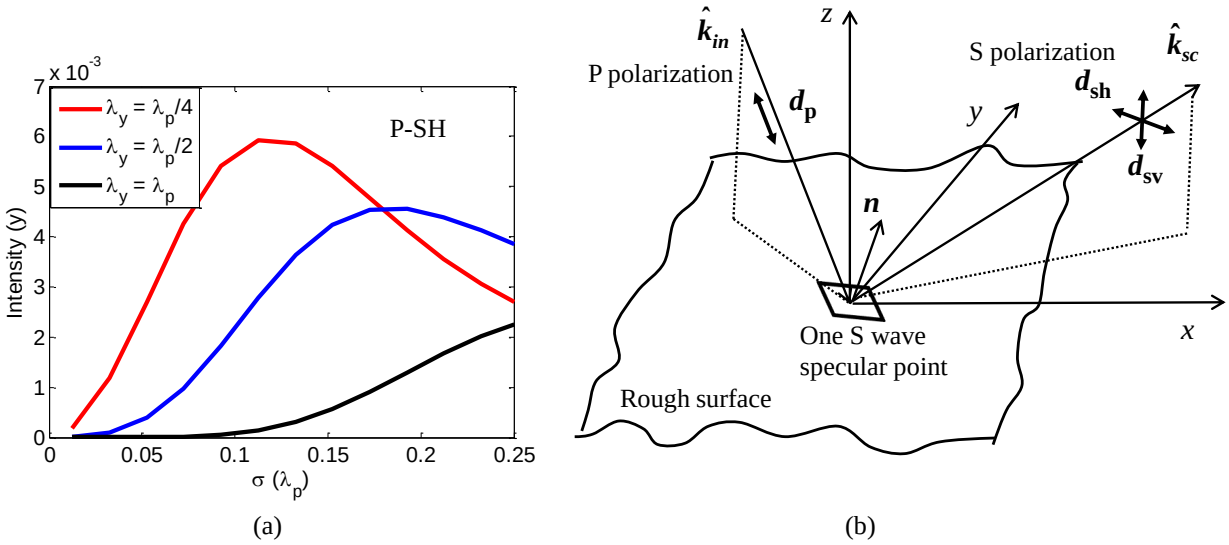

Figure 13: (a) Scattering intensity $< I_{y,ps} >$ as a function of σ for different correlation lengths in the y- direction. (b) Sketch of the S wave specular point to illustrate the depolarization of the SH mode

investigated since it is the main feature of the depolarization. As noticed in Eq. (22), the coherent component for $I_{y,ps}$ is zero if $L_y \to \infty$, and hence the depolarization is purely contributed from the diffuse field. The scattering patterns of the SH mode from low to high roughness are shown in Fig. 5(c) and Fig. 6(c), respectively. The increased roughness causes a considerable shift of two symmetric peaks from $\theta_{sx} = 90^o, |\theta_{sz}| = 25^o$ roughly to $\theta_{sx} = 115^o, |\theta_{sz}| = 50^o$. Figure. 13 shows $I_{y,ps}$ as a function of the RMS value when $\theta_{sx} = 90^o, |\theta_{sz}| = 45^o$, with different out-of-plane correlation lengths λ_y when $\lambda_x = \lambda_p/2$. As λ_y increases the SH mode intensity decays quickly, and the decay is more prominent when λ_y reaches one wavelength. It is because in this manner the surface is becoming smoother in the y- direction. As can be imagined in the extreme situation when $\lambda_y \to \infty$, the SH mode intensity would vanish since no depolarization takes place.

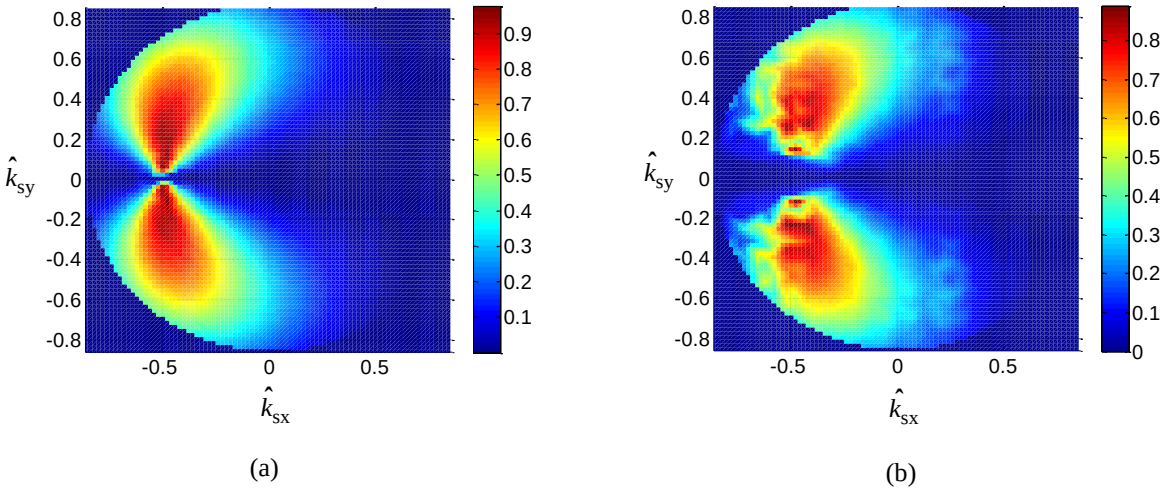

Figure 14: Depolarization pattern in terms of $\hat{k_{sx}}$ and $\hat{k_{sy}}$ when $\theta_{ix} = 180^o, \theta_{iz} = 30^o$. (a) Diffuse intensity. (b) Total intensity when $\sigma = \lambda_p/30$

To quantify how the SH polarization deviates from the SV polarization when the roughness in the y- direction is imposed, a depolarization factor is defined here for the scattered S waves, as the ratio between the out-of-plane intensity and the sum of all the components of intensities:

$$Q = I_{y,ps}/I_{ps} \tag{32}$$

According to Eq. (22), the finite sum of the exponential terms can be cancelled when dividing $I_{y,ps}$ by I_{ps} in Eq. (32). Only the angular factors are left and the depolarization factor for the diffuse intensity in Eq. (32) is simplified to:

$$Q = F^2_{y,ps}/F^2_{ps} \tag{33}$$

Eq. (33) indicates that the depolarization factor for the diffuse field does not rely on the roughness, and it is only a function of the incidence/scattering angle and the S-to-P wave speed ratio. In fact, according to the slope approximation, the scattered waves are mainly contributed from the 'specular points′, especially for the diffuse field. Hence, the polarization vectors for the scattered waves physically should be the same as those from 'specular points′ for the S mode as

shown in Fig. 13(b). As a result, the 3D depolarization factor determined by the polarization vector is also the same as that from the 'specular points', and hence for the diffuse field it is independent of the actual value of the roughness.

Figure 14(a) shows the diffuse wave depolarization factor as a function of the scattering angles in 3D, with a 30^o oblique incident wave within the x-z plane. Note that the depolarization factor is only a constant for the diffuse field with respect to the roughness, when the coherence effects are not included. For the total field (e.g. coherent intensity + diffuse intensity) the depolarization factor would be a function of the roughness, which is shown in Fig. 14(b) for slightly rough surfaces when $\sigma = \lambda_p/30$. As noticed in Eq. (22), the polarization vector of the coherent intensity is the same as that from the flat surface, which is only limited in the x-z plane if the surface is ideally infinitely long in the y- direction. However, in reality the surface has finite dimensions so that the polarization for the coherent intensity relies on the length of the surface in the y- direction. Therefore the polarization of the total intensity is somewhat affected by the coherent field. However, it is noticed that the overall shape of the depolarization for the total field is very similar to that for the diffuse field. The similarity is because the coherent contribution is mainly at the specular angles where the diffuse intensity $I_{y,ps}$ almost vanishes. According to Eq. (32), the depolarization in the specular direction would be almost zero, and hence the coherent field does not change the main shape of the depolarization pattern.

7. Conclusions and future work

In this article, we present an elastodynamic theory to predict the expected scattering intensity, especially the diffuse field from randomly rough surfaces, for the first time. Slope approximations are applied assuming 'specular points' for different modes, which enables the analytical manipulation of the ensemble averaging of the diffuse intensity as well as a high frequency asymptotic solution.

The theory is verified by comparison with numerical Monte Carlo simulations and experimental measurements, within the valid region of the Kirchhoff assumption. In particular, the effects of the roughness on the mode conversion, and consequently on the scattering intensity, are discussed.

It is found that a considerable proportion of the incident P waves convert to scattering S waves, and this is very strong around the specular angle. The mode conversion effect increases as the surface appears to be more rough, which results in unique scattering patterns for different modes. For instance, a remarkable peak around the backward angle is seen for the P-P mode for surfaces with a high roughness, and the P-S mode shows a dipole-like scattering pattern.

In addition, the 3D roughness-induced out-of plane SH mode and the depolarization is quantitatively analyzed. The amplitude of the out-of-plane intensity is found to depend on the roughness, and in particular it is very sensitive to the out-of-plane correlation length. In contrast, the depolarization factor remains a constant with respect to the roughness for the diffuse field.

The new capability to calculate the expected intensity, comprising both coherent and diffuse components, offers significant potential for applications in the authors' specialist field, NDE. Current thresholds for expected scattering intensities from rough defects are based on solely the coherent scattered field, and are thus rather conservative, and limited to the specular reflection direction. The additional intensity of the diffuse field, now quantifiable by this new approach, can increase the expected intensity substantially, thus eroding the conservatism while remaining safe. Furthermore, in some directions, such as the back-scatter direction, the intensity that can now be expected reliably, is dramatically higher, possibly enabling new choices of transducer placement and paths of insonification. In this article only the mean intensity is shown, and in a practical situation the standard deviation of the intensity is also important, as it offers the knowledge of confidence for the inspection of a single surface.

The standard deviation can be calculated using the Monte Carlo simulations, such as the results shown by Pettit et al. (2015). Alternatively one may seek to derive analytical expressions for the second moment (variance) of the intensity.

References

Achenbach, J.D., 2003. Reciprocity in elastodynamics. Cambridge University Express, Cambridge, UK.

Beckmann, P., Spizzichino, A., 1987. The scattering of electromagnetic waves from rough surfaces. Artech House, INC., London, UK.

Drinkwater, B.W., Wilcox, P.D., 2006. Ultrasonic arrays for non-destructive evaluation: A review. NDT & E Int. 39, 525–541.

Eckart, C., 1953. The scattering of sound from the sea surface. J. Acoust. Soc. Am. 25, 566–570.

Harper, E.Y., Labianca, F.M., 1975. Perturbation theory for scattering of sound from a point source by a moving rough surface in the presence of refraction. J. Acoust. Soc. Am. 57, 1044–1051.

Jarvis, A.J.C., Cegla, F.B., 2012. Application of the distributed point source method to rough surface scattering and ultrasonic wall thickness measurement. J. Acoust. Soc. Am. 132, 1325–1335.

Kodis, R.D., 1966. A note on the theory of scattering from an irregular surface. IEEE Trans. Antennas. Propag. 14, 77–82.

Makinde, W., Cristini, N.F., d. Bazelaire, E., 2005. Numerical modelling of interface scattering of seismic wavefield from a random rough interface in an acoustic medium: comparison between 2D and 3D cases. Geophys. Prospect. 53, 373–397.

Maznev, A.A., 2015. Boundary scattering of phonons: Specularity of randomly rough surface in the small-perturbation limit. Phys. Rev. B: Condens. Matter 91, 1–9.

Ogilvy, J.A., 1986. Theoretical comparison of ultrasonic signal amplitudes from smooth and rough defects. NDT & E Int. 19, 371–385.

Ogilvy, J.A., 1988. Computer simulation of acoustic wave scattering from rough surfaces. J. Phys. D: Appl. Phys. 21, 260–277.

Ogilvy, J.A., 1989. Model for the ultrasonic inspection of rough defects. Ultrasonics 27, 69–79.

Ogilvy, J.A., 1991. Theory of Wave Scattering from Random Rough Surfaces. Adam Hilger Ltd., Bristol, UK.

Ogilvy, J.A., Culverwell, I.D., 1991. Elastic model for simulating ultrasonic inspection of smooth and rough defects. Ultrasonics 29, 490–496.

Pettit, J., Walker, A.E., Lowe, M.J.S., 2015. Improved detection of rough defects for ultrasonic nondestructive evaluation inspections based on finite element modeling of elastic wave scattering. IEEE Trans. Ultrason. Ferroelectr. Freq. Control. 62, 1797–1808.

Rajagopal, P., Drozdz, M., Skelton, E.A., Lowe, M.J.S., Craster, R.V., 2012. On the use of absorbing layers to simulate the propagation of elastic waves in unbounded isotropic media using commercially available finite element packages. NDT & E Int. 51, 30–40.

Roberts, R.A., 2012. The effect of crack morphology on ultrasonic response. In D.O. Thompson, D.E. Chimenti, eds., Review of Progress in Quantitative NDE, vol. 1430 of AIP Conference Proceedings. American Institute of Physics, Denver, CO, 150–157.

Robertsson, J.O.A., Laws, R., Chapman, C., Vilotte, J.P., Delavaud, E., 2006. Modelling of scattering of seismic waves from a corrugated rough sea surface: a comparison of three methods. Geophys. J. Int. 167, 70–76.

Schmerr, L.W., Song, S.J., 2007. Ultrasonic Nondestructive Evaluation Systems: Models and Measurements. Springer, New York, USA.

Shi, F., Choi, W., Skelton, E.A., Lowe, M.J.S., Craster, R.V., 2015. The validity of Kirchhoff theory for scattering of elastic waves from rough surfaces. Proc. R. Soc. A 471, 1–19.

Sun, H., Pipe, K.P., 2012. Perturbation analysis of acoustic wave scattering at rough solid-solid interface. J. Appl. Phys. 111, 1–6.

Thorsos, E.I., 1988. The validity of the Kirchhoff approximation for rough surface scattering using a Gaussian roughness spectrum. J. Acoust. Soc. Am. 83, 78–92.

Thorsos, E.I., 1990. Acoustic scattering from a 'Pierson-Moskowitz' sea surface. J. Acoust. Soc. Am. 88, 335–349.

Thorsos, E.I., Jackson, D.R., 1989. The validity of the perturbation approximation for rough surface scattering using a Gaussian roughness spectrum. J. Acoust. Soc. Am. 86, 261–277.

Zhang, J., Drinkwater, B.W., Wilcox, P.D., 2011. Longitudinal wave scattering from rough crack-like defects. IEEE Trans. Ultrason. Ferroelectr. Freq. Control. 58, 2171–2180.

Zhang, J., Drinkwater, B.W., Wilcox, P.D., 2012. Effect of roughness on imaging and sizing rough crack-like defects using ultrasonic arrays. IEEE Trans. Ultrason. Ferroelectr. Freq. Control. 59, 939–948.